

Boosted Z-scheme photocatalytic overall water splitting with faceted Bi₄TaO₈Cl crystals as water oxidation photocatalyst

Shufang Chang ^{a,c,1}, Li Shi ^{d,1}, Jinxing Yu ^{a,b}, Ran Wang ^{a,b}, Xiaoxiang Xu ^{a,b,*}, Gang Liu ^{e,f,**}

^a Clinical and Central Lab, Putuo People's Hospital, Tongji University, Shanghai 200060, China

^b Shanghai Key Lab of Chemical Assessment and Sustainability, School of Chemical Science and Engineering, Tongji University, Shanghai 200092, China

^c School of Materials Science and Engineering, Shanghai Institute of Technology, Shanghai 201418, China

^d Jiangsu Key Lab for Organic Electronics and Information, Displays & Institute of Advanced Materials, School of Materials Science and Engineering, Nanjing University of Posts and Telecommunications, Nanjing 210023, China

^e Shenyang National laboratory for Materials Science, Institute of Metal Research, Chinese Academy of Science, Shenyang 110016, China

^f School of Materials Science and Engineering, University of Science and Technology of China, Shenyang 110016, China



ARTICLE INFO

Keywords:
Facet-engineering
Bi₄TaO₈Cl
Water oxidation
Z-scheme
Photocatalysis

ABSTRACT

We have identified a facet-assisted mechanism for photocarrier separation in flux-treated Bi₄TaO₈Cl crystals that expose mainly {001} and {110} facets. These two crystal facets have different energy states that provide an internal electric field to split photocarriers towards different crystal facets. We have further leveraged the phenomenon by facet-selective deposition of CoO_x cocatalyst at {001} crystal facets where holes are accumulated to expedite interfacial charge transfer reactions. The coupling of these two facet-engineering techniques brings exquisite control over the flow of photocarriers which cascade continuously from bulk to the surface for catalytic reactions. Under optimal conditions, the CoO_x-deposited Bi₄TaO₈Cl achieves an unprecedentedly high apparent quantum efficiency of 27% at 420 ± 20 nm for water oxidation into O₂. Stable overall water splitting into H₂ and O₂ (molar ratio 2:1) under visible light irradiation has also been realized in a Z-scheme system employing the CoO_x-deposited Bi₄TaO₈Cl as the O₂-evolution moiety.

1. Introduction

Conversion of solar power into the form of clean fuel H₂ by photocatalytic water splitting holds the great promise to address worldwide concerns on energy security and environmental degradations [1–6]. Although water splitting can be achieved efficiently in some UV-illuminated wide bandgap semiconductors [7,8], it occurs to be rather difficult for narrow bandgap semiconductors that can take advantage of most solar photons. There are often competitive tensions, for instance, the bandgap is narrowed at the expense of photocarrier energetics [9]. Great efforts thus have to be devoted to accelerating photocarrier separation and transfer steps so as to compensate for the decreased energetics of these photocarriers.

As mixed-anion compounds, Bi₄MO₈X (M = Nb, Ta; X = Cl, Br) delivers exceptional stability for photocatalytic water oxidation into O₂

under visible light illumination [10]. The structure of Bi₄MO₈X contains regular layer-stacking of the type [Bi₂O₂][MO₄][Bi₂O₂][X], representing as the simplest member of Sillén-Aurivillius intergrowth compounds [11,12]. Their superior stability and visible light sensitivity stem from the destabilized oxygen in the fluorite-type [Bi₂O₂] layers that upshifts the valence band maximum according to the previous reports [13–15]. Nevertheless, the photocatalytic behavior of Bi₄MO₈X (M = Nb, Ta; X = Cl, Br) is susceptible to a wealth of synthetic parameters [16–21]. In particular, samples prepared by chloride-assisted flux method normally exhibit better photocatalytic performance than those from conventional solid-state reactions [22]. High crystallinity and fewer Cl vacancies have been identified as the possible reasons for such improved activity [23]. However, little is known about the separation and distribution of photocarriers in these flux-treated samples, let alone the strategies to further enhance their photocatalytic activity.

* Corresponding author at: Clinical and Central Lab, Putuo People's Hospital, Tongji University, Shanghai 200060, China.

** Corresponding author at: Shenyang National laboratory for Materials Science, Institute of Metal Research, Chinese Academy of Science, Shenyang 110016, China.

E-mail addresses: xxxu@tongji.edu.cn (X. Xu), gangliu@imr.ac.cn (G. Liu).

¹ These authors contribute equally to this work

In this work, we have identified a facet-assisted mechanism for photocarrier separation in flux-treated $\text{Bi}_4\text{TaO}_8\text{Cl}$. We have further leveraged the phenomenon to enhance the photocatalytic activity by facet-selective deposition of the cocatalyst. The coupling of these two facet-engineering techniques brings precise control over the separation and transfer steps of photocarriers, which in turn, delivers exceptional performance for photocatalytic water oxidation into O_2 . The application of this promising photocatalyst has also been exemplified by integrating CoO_x -loaded $\text{Bi}_4\text{TaO}_8\text{Cl}$ into a Z-scheme system which can stably split water into stoichiometric H_2 and O_2 under both visible light and simulated AM1.5 illumination.

2. Experimental

2.1. Synthesis of sample powders

$\text{Bi}_4\text{TaO}_8\text{Cl}$ powders were prepared by two different methods, namely molten-salt-based flux method and conventional solid-state reactions. For both methods, BiOCl was used as a precursor and was prepared according to a previous report [24]. For the flux method, 0.3141 g as-prepared BiOCl , 0.6530 g Bi_2O_3 (Aladdin, 99.9%), and 0.2210 g Ta_2O_5 (Aladdin, 99.99%) were thoroughly mixed up with 2.9279 g NaCl (Aladdin, 99.9%) and 3.7463 g KCl (Aladdin, 99.9%). The admixtures were transferred into an alumina crucible and were calcined in a muffle furnace at 973 K for 14 h. After cooled naturally to room temperature, the resultant powders were washed repeatedly with deionized water to remove the chloride salt and were dried in an oven at 353 K for 5 h. The so-formed $\text{Bi}_4\text{TaO}_8\text{Cl}$ powders were denoted as $\text{Bi}_4\text{TaO}_8\text{Cl-F}$. For solid-state reactions, the raw materials and calcination conditions were kept the same except that NaCl and KCl were not added. The $\text{Bi}_4\text{TaO}_8\text{Cl}$ powders obtained were denoted as $\text{Bi}_4\text{TaO}_8\text{Cl-S}$ for discrimination. Rh-doped powders (i.e. $\text{SrTiO}_3\text{-Rh}$) were synthesized according to a previous report [25]. The $\text{SrTiO}_3\text{-Rh}$ powders were loaded with 0.5 wt% Ru nanoparticles to promote the water reduction reaction. The loading procedures followed a previous report [26].

2.2. Photo-deposition experiments over $\text{Bi}_4\text{TaO}_8\text{Cl-F}$

Mn^{2+} and Pb^{2+} cations are easily oxidized by photo-generated holes to form MnO_x and PbO_2 precipitates. Thereby, these cations serve as effective chemical probes to detect the location of holes. In this work, 50 mg freshly prepared $\text{Bi}_4\text{TaO}_8\text{Cl-F}$ powders were dispersed into 15 mL MnCl_2 or $\text{Pb}(\text{NO}_3)_2$ aqueous solution (0.3 mg/mL). 0.1 g NaIO_3 was also added as an electron scavenger. The so-formed suspensions were irradiated by a 300 W Xenon lamp (PLX-SX300, Perfect Light) for 5 h. The suspensions were centrifuged, rinsed with deionized water, and dried at 353 K overnight.

PtCl_6^{2-} anions can be easily reduced into Pt nanoparticles by photo-generated electrons. Thereby, these anions are useful indicators for the detection of electron location. In this work, 50 mg freshly prepared $\text{Bi}_4\text{TaO}_8\text{Cl-F}$ powders were dispersed into 10 mL H_2PtCl_6 aqueous solution (0.5 mg/mL). 5 mL methanol was also added as a hole scavenger. The so-formed suspensions were irradiated by a 300 W Xenon lamp (PLX-SX300, Perfect Light) for 5 h. The suspensions were centrifuged, rinsed with deionized water, and dried at 353 K overnight.

For the detection of both electron and hole locations, $\text{Bi}_4\text{TaO}_8\text{Cl-F}$ powders deposited with MnO_x were subsequently deposited with Pt according to the above procedures.

2.3. Deposition of CoO_x cocatalyst for water oxidation

CoO_x was applied as a cocatalyst to facilitate water oxidation reactions and was deposited by three different methods, i.e. hydrothermal method, photo-deposition method, and thermal decomposition method. For the hydrothermal method, 0.2 g $\text{Bi}_4\text{TaO}_8\text{Cl-F}$ powders, calculated amounts of $\text{Co}(\text{NO}_3)_2 \cdot 6 \text{ H}_2\text{O}$ (Aladdin, 99.9%) and 0.0016 g urea

(Aladdin, 99.5%) were dispersed into 30 mL deionized water. The resultant suspensions were transferred into a Teflon-lined stainless steel autoclave and were heated at 393 K for 5 h. The precipitants were centrifuged, rinsed with deionized water, and calcined in the N_2 atmosphere at 673 K for 1 h. The so-formed sample powders were labeled as $\text{CoO}_x(\text{H})@\text{Bi}_4\text{TaO}_8\text{Cl-F}$. CoO_x content was controlled by varying the amounts of $\text{Co}(\text{NO}_3)_2 \cdot 6 \text{ H}_2\text{O}$ used. For the photo-deposition method, 0.2 g $\text{Bi}_4\text{TaO}_8\text{Cl-F}$ powders, 0.1 g NaIO_3 , and 4 mg $\text{Co}(\text{NO}_3)_2 \cdot 6 \text{ H}_2\text{O}$ were dispersed into 100 mL deionized water. The resultant suspensions were illuminated by a 300 W Xenon lamp for 10 min. The precipitants were then rinsed repeatedly with deionized water and were dried at 353 K overnight. The product was labeled as $\text{CoO}_x(\text{P})@\text{Bi}_4\text{TaO}_8\text{Cl-F}$. For the thermal decomposition method, 0.2 g $\text{Bi}_4\text{TaO}_8\text{Cl-F}$ powders were dispersed into 5 mL $\text{Co}(\text{NO}_3)_2$ aqueous solution. The resultant suspensions were heated on a hotpot until dry and were calcined in air at 623 K for 2 h. The so-formed sample powders were labeled as $\text{CoO}_x(\text{T})@\text{Bi}_4\text{TaO}_8\text{Cl-F}$. CoO_x content was controlled by adjusting the concentration of $\text{Co}(\text{NO}_3)_2$ aqueous solution.

2.4. Material characterizations

All synthesized sample powders were analyzed by X-ray powder diffraction (XRD) technique to examine phase composition. A Bruker D8 Focus diffractometer with $\text{Cu K}_{\alpha 1}$ ($\lambda = 1.5406 \text{ \AA}$) and $\text{Cu K}_{\alpha 2}$ ($\lambda = 1.5444 \text{ \AA}$) radiation was used for XRD analysis. The microstructures of sample powders were inspected by a field emission scanning electron microscope (Hitachi S4800, Japan) and a transmission electron microscope (JEOL JEM-2100, Japan). The specific surface area of sample powders were analyzed on a NOVA 2200e adsorption instrument and were calculated based on Brunauer-Emmett-Teller (BET) model. UV-vis diffuse reflectance spectra were collected on a UV-vis spectrophotometer coupled with an integrating sphere (JASCO-750). JASCO spectralon plate was used for baseline correction. The surface conditions of sample powders were investigated by X-ray photoelectron spectroscopy (XPS) analysis (Thermo Escalab 250, monochromatic Al K_{α} source). XPS data collected were adjusted according to the adventitious carbon C 1 s peak at 284.7 eV. Overlapping peaks were fitted using the XPS PEAKFIT software in which a Gaussian-Lorentzian function (Lorentzian weighting of 20%) and a Shirley-type background were used for fitting. The photoluminescence (PL) spectra were collected on a fluorescence spectrophotometer (F-7000, Hitachi). UV photons with a wavelength of 340 nm were used as the excitation source. Time-resolved PL decay spectra were acquired on a Horiba FL-1016 spectrophotometer using a 340 nm nanosecond pulse laser as the excitation source and were collected at PL peak position. The soft X-ray absorption spectra (XAS) were collected at the BL10B station of the National Synchrotron Radiation Laboratory (NSRL, Hefei, P. R. China).

2.5. Photocatalytic reactions

The photocatalytic properties of sample powders were evaluated by monitoring their O_2 -evolution from water under visible light illumination ($\lambda \geq 420 \text{ nm}$). All experiment was carried out using a top-irradiation-type reactor connected to a gas-closed circulation and evacuation system (Labsolar-IIIAG, Perfect Light). For a typical experiment, 25 mg sample powders were dispersed into 100 mL silver nitrate aqueous solution (0.05 M). The suspensions were transferred into the reactor and were subject to evacuation for 45 min to eliminate air dissolved. A 300 W Xenon lamp (PLX-SX300, Perfect Light) coupled with a UV cutoff filter ($\lambda \geq 420 \text{ nm}$) was adopted to generate a visible light beam. The gas evolved during the experiment was determined by on-line gas chromatography (TECHCOMP, GC7900) coupled with a thermal conductivity detector and 5 Å molecular sieve columns. The carrier gas was high purity Ar (Jiaya Chemicals, 99.999%). For the determination of apparent quantum efficiency (AQE), monochromatic light was used and was produced by filtering the output of the 300 W Xenon lamp (PLX-

SX300, Perfect Light) with a bandpass filter at 420 nm, 450 nm, 500 nm, 550 nm, and 600 nm. The photon flux at individual wavelength was gauged by a quantum meter (Apogee MP-300, USA) (See Table S2). The AQE at each wavelength was then calculated using the following equation:

$$\text{AQE} = 4 \times \text{mol of oxygen production per hour/mol of photon flux per hour} \times 100\%.$$

For Z-scheme type overall water splitting reactions, 50 mg SrTiO₃:Rh powders (loaded with 0.5 wt% Ru), 50 mg CoO_x(H)_n@Bi₄TaO₈Cl-F powders (loaded with 2 wt% CoO_x) were dispersed into the reactor containing 100 mL FeCl₃ aqueous solution (2 mM). The pH of the suspension was adjusted to 2.5 by adding HCl aqueous solution (1 M). The experimental conditions for gas analysis within the reactor were the same as above.

2.6. Photoelectrochemical (PEC) measurements

The photocatalytic behavior of sample powders was further explored based on PEC analysis. For PEC measurements, sample powders were deposited onto fluorine-doped tin oxide (FTO) glass to fabricate semiconductor photoelectrodes according to previous reports [27,28]. The as-prepared photoelectrode, Pt foil (1 × 1 cm) and the Ag/AgCl reference electrode were immersed into K₃PO₄/K₂HPO₄ (25 mL, 0.1 M, pH = 12.66) aqueous solution to configure a three-electrodes setup. The setup was connected to a Zahner electrochemical workstation for PEC analysis. A 300 W Xenon lamp (PLX-SXE300, Perfect Light) was used as the light source. The visible light beam was generated by filtering the output of the lamp with a UV cutoff filter ($\lambda > 420$ nm) and illuminated the backside of the FTO-based photoelectrode during PEC measurements. Electrochemical impedance spectra data were collected from 10⁵ Hz to 0.1 Hz with AC amplitude of 10 mV. Charge separation efficiency and interfacial charge transfer efficiency were determined based on previous reports by measuring the photocurrent with or without Na₂SO₃ [29,30].

2.7. Theoretical calculations

All the spin-polarized DFT calculations were performed on the Vienna ab-initio simulation package (VASP) [31,32]. The exchange-correlation was described by Perdew-Burke-Ernzerhof (PBE) functional within the generalized gradient approximation (GGA) [33, 34], and the valence electron configurations were described by the projector augmented wave (PAW) method [35]. The {001} and {110} facets of cubic Bi₄TaO₈Cl were constructed to explore electronic properties. Both {001} and {110} facets contain at least five atomic layers, which are thick enough for energy convergence. The valence electronic wave function was expanded on a plane-wave basis set with a cutoff of 450 eV. All the structures were fully relaxed until the force on each atom (except for the fixed twos) was less than 0.02 eV/Å and the convergence criterion for the electronic structure iteration was set to be 10⁻⁵ eV. A Monkhorst-Pack k-points mesh of 7 × 7 × 1 and 2 × 7 × 1 was sampled for {001} and {110} facets, respectively. A vacuum thickness of 20 Å was placed along the vertical direction of the surface to avoid interaction between periodic units.

2.8. Photocarrier distribution simulation

The distribution of photocarriers in Bi₄TaO₈Cl-F before and after CoO_x deposition was simulated using the semiconductor module of COMSOL Multiphysics software. For simplicity, a two-dimensional brick model was constructed to represent the cross-section of Bi₄TaO₈Cl-F plate-like particles. The geometric size of the model was estimated according to FE-SEM image of Bi₄TaO₈Cl-F particles. The semiconductor parameters used for simulations are tabulated in Table S3. A finite volume method employing Scharfetter-Gummel discretization was used for the numerical calculation of particle transport [36]. Photocarriers were assumed to be generated uniformly in the model due to the severe

reflection and scattering events for randomly oriented particles. The photocarrier recombination was considered to be Shockley-Reed-Hall type one which is mediated by defects. The contact between cocatalyst and Bi₄TaO₈Cl-F was assumed to be ohmic while the Bi₄TaO₈Cl-F/electrolyte interfaces are set to be ideal Schottky type junctions. The models were discretized by very fine mesh upon which the simulation was carried out by solving the Poisson, drift-diffusion, and current continuity equations in a self-consistent manner at the individual discretized node.

3. Results and discussions

3.1. Crystal structure, microstructures and photocatalytic activity

Two different methods including molten-salt-based flux method and conventional solid-state reactions were introduced to synthesize Bi₄TaO₈Cl. The product powders were subsequently labeled as Bi₄TaO₈Cl-F and Bi₄TaO₈Cl-S for discrimination, respectively. Both methods generate single-phase Bi₄TaO₈Cl powders as indicated by XRD analysis (Fig. 1a). Although these powders show identical XRD reflection positions, they have clear distinctions in reflection intensity. For instance, Bi₄TaO₈Cl-F has much stronger {00l} reflections than Bi₄TaO₈Cl-S, suggesting a preferential growth of {001} crystal facets in its particles. This is confirmed by microscopic inspections. Unlike Bi₄TaO₈Cl-S which contains irregularly shaped particles, Bi₄TaO₈Cl-F comprises plate-like particles according to their FE-SEM images (Fig. 1c-d). Each Bi₄TaO₈Cl-F particle is a single crystal with its top flat surface oriented along [001] direction, exposing mainly {001} and {110} crystal facets, as indicated by selected area electron diffraction (SAED) and high-resolution TEM image (Fig. S1). Molten-salt-based flux method produces a liquid synthetic environment that favors grain growth following the crystal habit of the layered structure of Bi₄TaO₈Cl. UV-vis DRS spectra suggest that Bi₄TaO₈Cl-S and Bi₄TaO₈Cl-F have quite different light absorption behavior above bandgap, likely due to the change of light reflecting/scattering properties as particle morphologies have been substantially modified, i.e. irregular to plate-like. Apart from the distinct morphologies, Bi₄TaO₈Cl-S and Bi₄TaO₈Cl-F have similar BET surface area (~ 2 m²/g) and bandgap (~ 2.55 eV) (Fig. 1b), being consistent with previous reports [14,16,17]. Despite these similarities, Bi₄TaO₈Cl-F is much more active than Bi₄TaO₈Cl-S in photocatalytic water oxidation into O₂ (Fig. 2a). Over a time span of 2.5 h, Bi₄TaO₈Cl-F produces more than twice as much O₂ as Bi₄TaO₈Cl-S without the assistance of a cocatalyst. The origin of O₂ is confirmed from water oxidation reactions by an isotope-labeled control experiment (Fig. 2b). Since no cocatalyst is used under these circumstances, such a high activity is inherently linked to the intrinsic property of Bi₄TaO₈Cl-F and is further explored.

3.2. Facet-assisted photocarrier separation

To elucidate the superior activity of Bi₄TaO₈Cl-F, the photocarrier separation conditions were investigated by a series of photo-deposition experiments that disclose the location of photocarriers (e⁻ and h⁺). MnO_x deposition as a result of Mn²⁺ oxidation has been used as a chemical probe to detect the position of holes. The flocculent MnO_x precipitants are exclusively found at the {001} crystal facets of Bi₄TaO₈Cl-F particles, suggesting that the holes selectively accumulate at {001} facets (Fig. 3a). A similar phenomenon is also observed in the PbO₂ deposition experiment (Fig. S2a), confirming that photo-oxidation reactions take place preferentially over {001} crystal facets. On the contrary, Pt deposition by PtCl₆²⁻ reduction occurs solely at {110} crystal facets (Fig. 3b), indicating that the electrons tend to segregate at {110} facets for reduction reactions. The distinct function of {001} and {110} facets are further verified in a dual photo-deposition experiment of both MnO_x and Pt (Fig. S2b). Photocarriers in Bi₄TaO₈Cl-F are therefore spatially separated by the exposed {001} and {110} facets which would

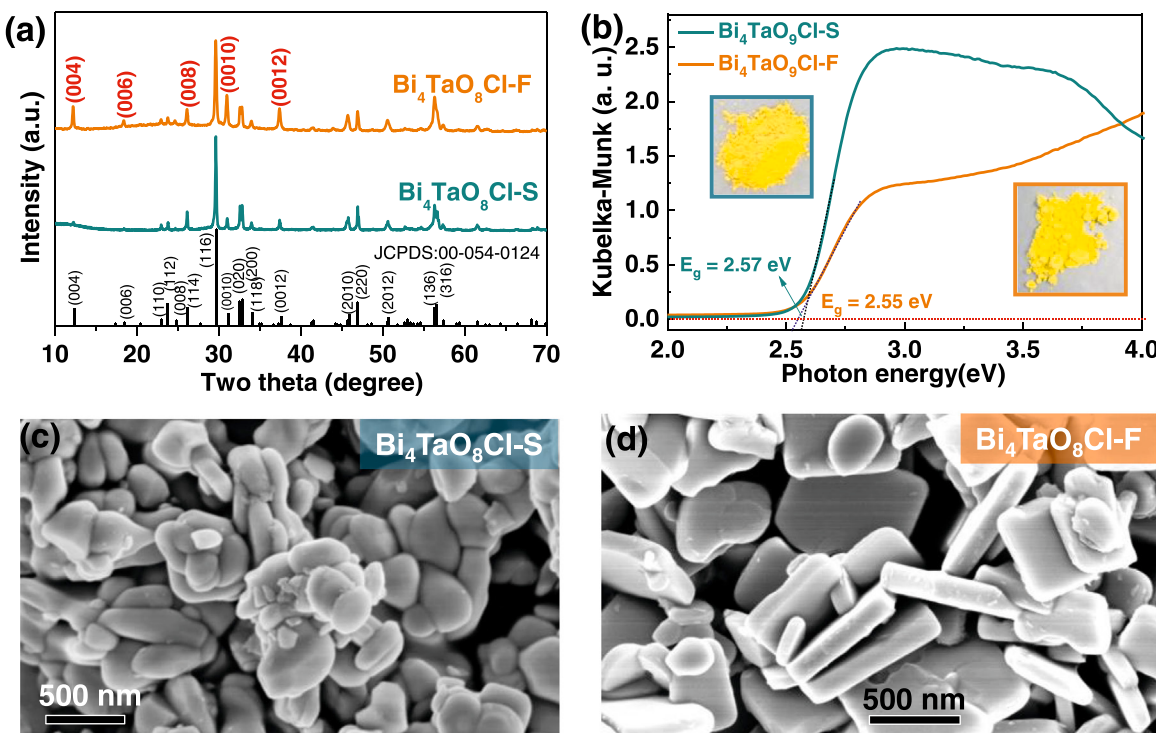


Fig. 1. (a) XRD patterns of $\text{Bi}_4\text{TaO}_8\text{Cl-F}$ and $\text{Bi}_4\text{TaO}_8\text{Cl-S}$, standard patterns of $\text{Bi}_4\text{TaO}_8\text{Cl}$ (JCPDS: 00-054-0124) are included for comparisons. (b) UV-vis DRS spectra of $\text{Bi}_4\text{TaO}_8\text{Cl-F}$ and $\text{Bi}_4\text{TaO}_8\text{Cl-S}$, insets show the digital photographs of sample powders. (c) FE-SEM image of $\text{Bi}_4\text{TaO}_8\text{Cl-S}$. (d) FE-SEM image of $\text{Bi}_4\text{TaO}_8\text{Cl-F}$.

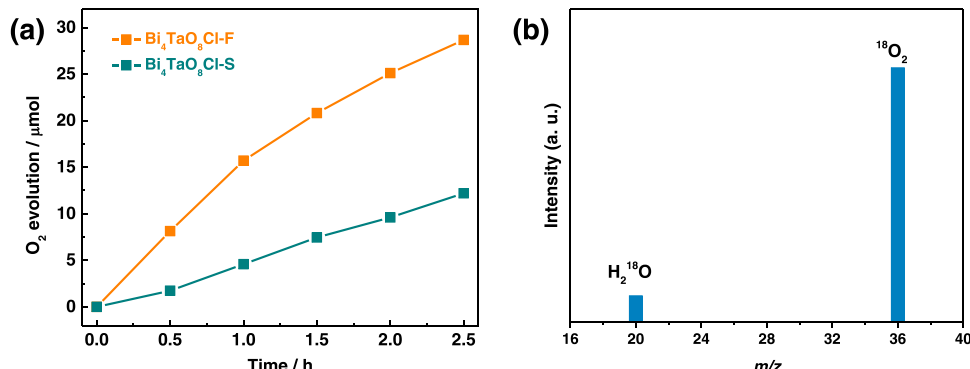


Fig. 2. (a) Photocatalytic O_2 -evolution profile of $\text{Bi}_4\text{TaO}_8\text{Cl-F}$ and $\text{Bi}_4\text{TaO}_8\text{Cl-S}$, no cocatalyst was loaded. (b) mass spectra of gas evolved from $\text{Bi}_4\text{TaO}_8\text{Cl-F}$ in the presence of H_2^{18}O under visible light illumination ($\lambda \geq 420 \text{ nm}$).

dramatically decrease the risk of photocarrier recombination.

Thanks to the facet-assisted photocarrier separation, $\text{Bi}_4\text{TaO}_8\text{Cl-F}$ now owns much-accelerated photocarrier dissociation than $\text{Bi}_4\text{TaO}_8\text{Cl-S}$, as supported by photoluminescence (PL) spectra, time-resolved PL decay spectra, and photoelectrochemical measurements. The PL spectra of both samples are characterized by a broad emission band centered at 490 nm, corresponding to the band edge emission of $\text{Bi}_4\text{TaO}_8\text{Cl}$ ($E_g \sim 2.55 \text{ eV}$). It is clear from PL spectra that $\text{Bi}_4\text{TaO}_8\text{Cl-F}$ shows much-damped band edge emission compared to $\text{Bi}_4\text{TaO}_8\text{Cl-S}$, indicative of much-decreased radiative recombination of photocarriers in $\text{Bi}_4\text{TaO}_8\text{Cl-F}$ [37]. Moreover, time-resolved PL decay spectra suggest that $\text{Bi}_4\text{TaO}_8\text{Cl-F}$ has substantially slower PL decay processes than $\text{Bi}_4\text{TaO}_8\text{Cl-S}$ at the band edge emission (Fig. 4b). The average PL decay lifetime is almost doubled from $\text{Bi}_4\text{TaO}_8\text{Cl-S}$ to $\text{Bi}_4\text{TaO}_8\text{Cl-F}$ (Table S1), corresponding to a significant increment of long-lived photocarriers [38]. Consistently, linear sweep voltammetry reveals that $\text{Bi}_4\text{TaO}_8\text{Cl-F}$ delivers much-higher photocurrent than $\text{Bi}_4\text{TaO}_8\text{Cl-S}$ under the same potential bias (Fig. 4c). The enhanced photocurrent of $\text{Bi}_4\text{TaO}_8\text{Cl-F}$

arises mainly from the improved charge separation efficiency as is derived with an aid of a sacrificial agent (Fig. 4d, Fig. S3). These results unequivocally suggest that photocarrier separation conditions in $\text{Bi}_4\text{TaO}_8\text{Cl}$ can be substantially improved by the selective exposure of $\{001\}$ and $\{110\}$ crystal facets.

An intuitive question arises as to how $\{001\}$ and $\{110\}$ crystal facets promote photocarrier separation in $\text{Bi}_4\text{TaO}_8\text{Cl-F}$. To address this question, we have performed a DFT calculation to obtain the electronic structures of $\{001\}$ and $\{110\}$ facets. After geometry optimization and surface formation energy test, it can be seen that $\{001\}$ and $\{110\}$ facets differ greatly in surface atomic arrangements (Fig. 5a). For instance, $\{001\}$ facets are terminated by Cl^- anions while $\{110\}$ facets have a high fraction of O^{2-} anions and Bi^{3+} cations at the outmost layer, indicating different surface energy states for these two crystal facets. This is confirmed by the projected density of states (PDOS) at $\{001\}$ and $\{110\}$ facets which depicts the levels of the conduction band (CB) and valence band (VB) (Fig. 5b). In sharp contrast to $\{001\}$ facets which show a “clean” band gap, $\{110\}$ facets are enriched in middle-gap states,

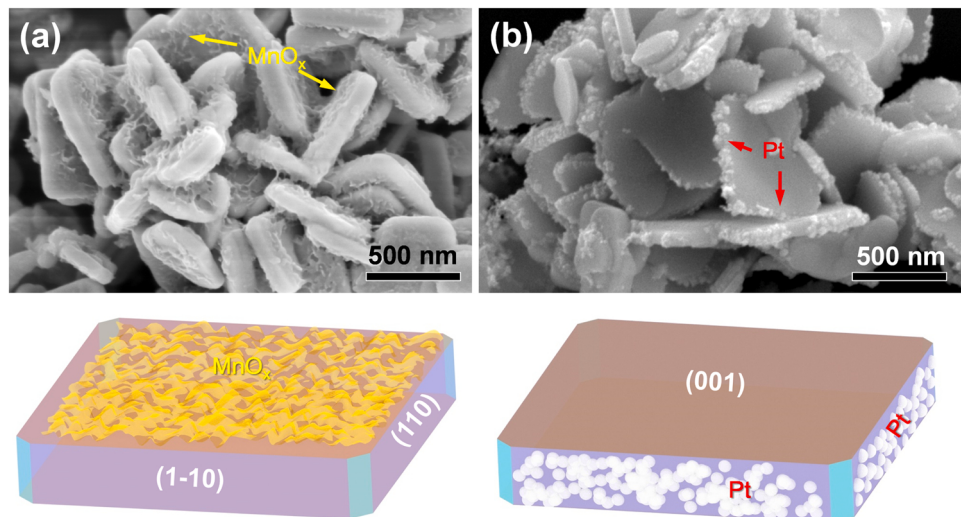


Fig. 3. (a) FE-SEM image of $\text{Bi}_4\text{TaO}_8\text{Cl-F}$ photo-deposited with MnO_x . (b) FE-SEM image of $\text{Bi}_4\text{TaO}_8\text{Cl-F}$ photo-deposited with Pt; location of MnO_x and Pt is schematically illustrated beneath the FE-SEM images.

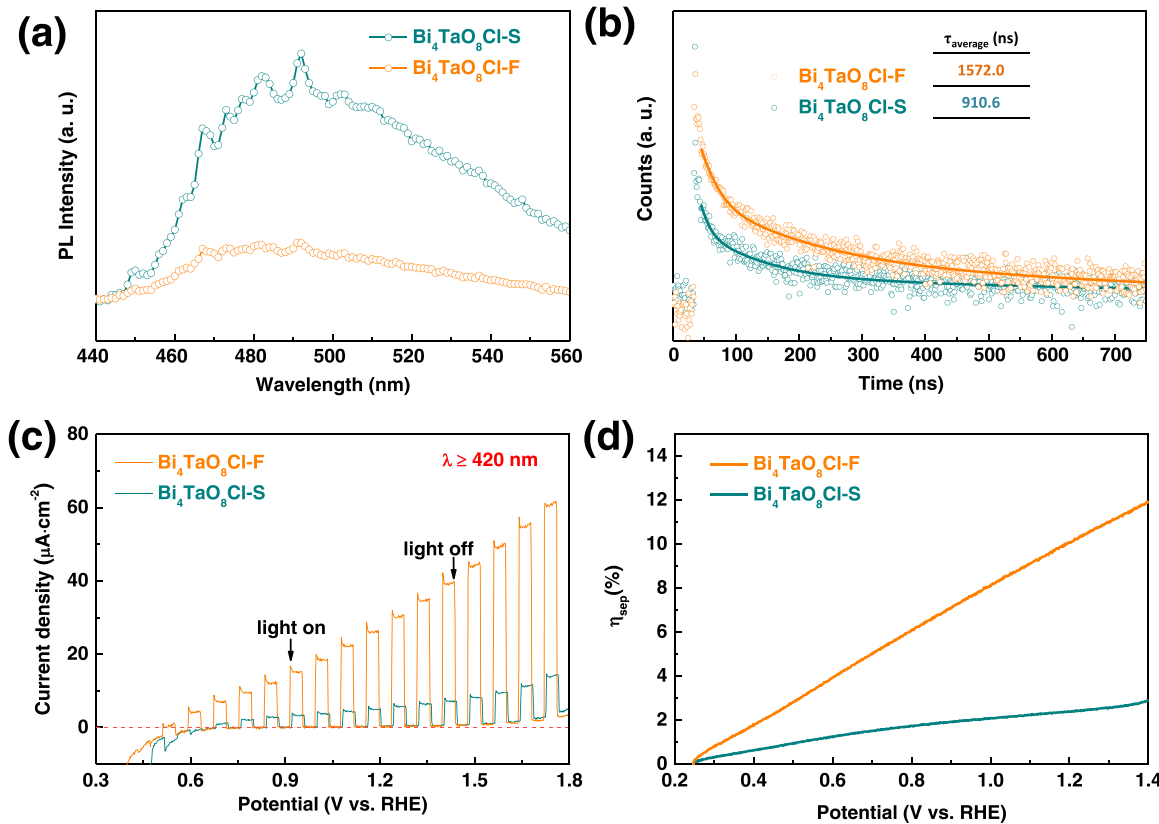


Fig. 4. (a) Photoluminescence (PL) spectra of $\text{Bi}_4\text{TaO}_8\text{Cl-F}$ and $\text{Bi}_4\text{TaO}_8\text{Cl-S}$. (b) time-resolved PL decay spectra of $\text{Bi}_4\text{TaO}_8\text{Cl-F}$ and $\text{Bi}_4\text{TaO}_8\text{Cl-S}$, amplitude-weighted average PL decay lifetime is tabulated as insets. (c) linear sweep voltammetry of $\text{Bi}_4\text{TaO}_8\text{Cl-F}$ and $\text{Bi}_4\text{TaO}_8\text{Cl-S}$ under chopped visible light illumination ($\lambda \geq 420 \text{ nm}$). (d) charge separation efficiency (η_{sep}) at different potential of $\text{Bi}_4\text{TaO}_8\text{Cl-F}$ and $\text{Bi}_4\text{TaO}_8\text{Cl-S}$, the values are deduced with an aid of Na_2SO_3 as a sacrificial agent according to a previous report [36].

corresponding to a variety of surface states. These middle-gap states have major contributions from Bi and O atomic orbitals (Fig. S4) thereby are linked to the exposed Bi^{3+} and O^{2-} ions at $\{110\}$ facets. Given the energy levels of different states in Fig. 5b, we can sketch the band edge positions at $\{001\}$ and $\{110\}$ facets which are illustrated in Fig. 5c. From the sketch, one can quickly realize that $\{001\}$ facets serve to accumulate photo-generated holes as their VB edge position is higher than that of

$\{110\}$ facets. The photo-generated electrons, however, will be collected by $\{110\}$ facets due to the presence of surface states. All these surface states have a lower energy position than the CB edge of both $\{001\}$ and $\{110\}$ facets thereby acting as an effective sink to store electrons. In other words, $\{001\}$ and $\{110\}$ facets now establish an internal electric field to separate photocarriers due to their different energy states at the surfaces. This charge separation mechanism resembles that of type-II

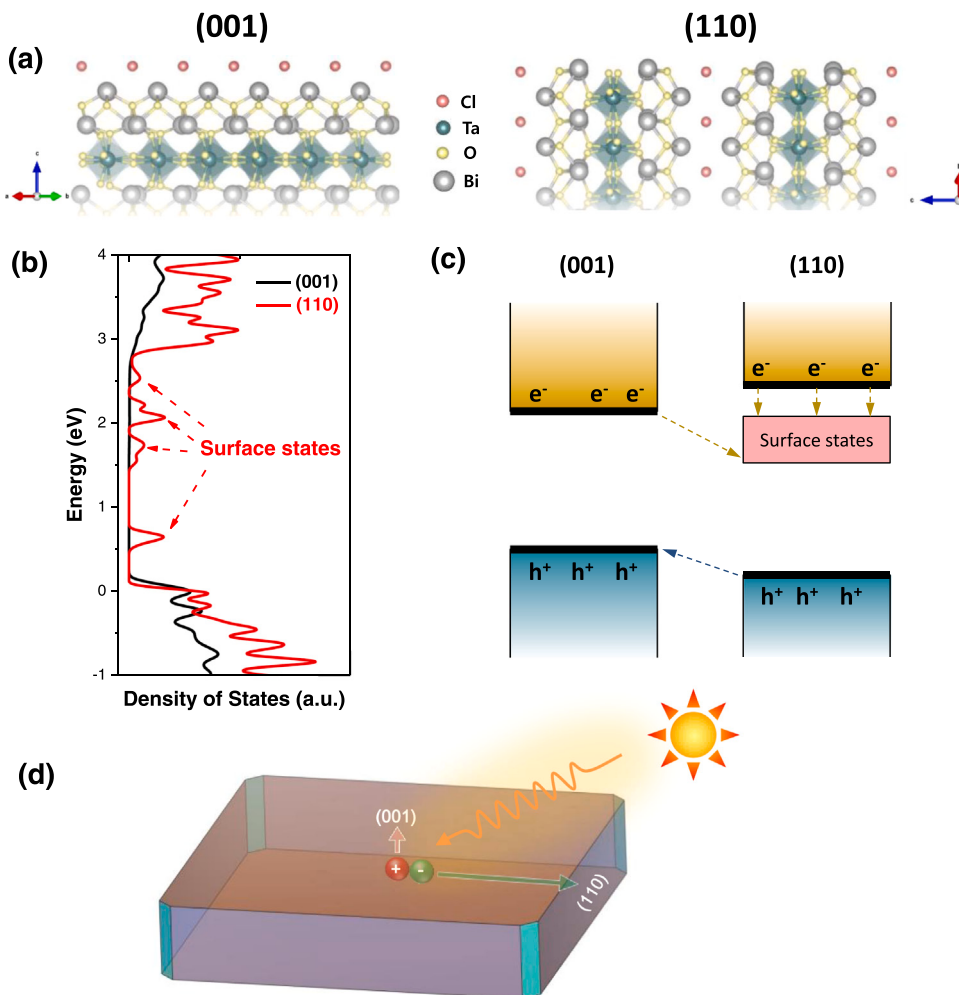


Fig. 5. (a) Side view of $\text{Bi}_4\text{TaO}_8\text{Cl}$ crystal structure exposing {001} and {110} facets. (b) projected density of states (PDOS) diagram from DFT calculations for {001} and {110} facets of $\text{Bi}_4\text{TaO}_8\text{Cl}$. (c) schematic illustration of band edge positions at {001} and {110} facets. (d) schematic illustration of photocarrier separation in $\text{Bi}_4\text{TaO}_8\text{Cl}-\text{F}$ particle enclosed by {001} and {110} facets.

semiconductor heterojunctions and is in good accordance with previous photo-deposition experiments that {001} facets collect holes whilst {110} facets are the destination for electrons. A diagram of photocarrier separation by {001} and {110} facets is illustrated in Fig. 5d. The photocarriers can be quickly dissociated and spatially separated to different crystal facets for different redox reactions. It is noteworthy that this charge separation mechanism also helps to explain the poor activity for photocatalytic H_2 evolution over $\text{Bi}_4\text{TaO}_8\text{Cl}-\text{F}$ [17]. The electrons are trapped by the surface states of {110} facets and may have inadequate energy to drive water reduction reactions.

3.3. Facet-selective cocatalyst deposition

Given the charge separation mechanism of $\text{Bi}_4\text{TaO}_8\text{Cl}-\text{F}$, we sought to leverage the facet-assisted charge separation by facet-selective deposition of cocatalyst to further enhance the photocatalytic performance. This was done by a hydrothermal method that deposits CoO_x nanoparticles selectively and homogeneously at {001} facets as can be seen from the FE-SEM image (Fig. 6a and Fig. S5). These CoO_x nanoparticles are firmly anchored over {001} facets in a face-to-face manner according to the TEM image (Fig. 6b). X-ray absorption spectra (XAS) analysis suggests that the deposited CoO_x nanoparticles are essentially CoO (Fig. S6) and high-resolution TEM analysis indicates that the CoO_x nanoparticles attached to $\text{Bi}_4\text{TaO}_8\text{Cl}-\text{F}$ through their {111} crystal facets (Fig. 6c and Fig. 6d). Such facet connections can be rationalized by the

strong columbic attraction between Co^{2+} -terminated {111} facets of CoO and Cl^- -terminated {001} facets of $\text{Bi}_4\text{TaO}_8\text{Cl}-\text{F}$. Contrary to the hydrothermal deposition method, conventional deposition methods, e.g. photo-deposition and thermal decomposition method, produce distinct microstructures between CoO_x and $\text{Bi}_4\text{TaO}_8\text{Cl}-\text{F}$ (Fig. S7). For instance, the photo-deposition method generates thin CoO_x layers selectively over {001} facets of $\text{Bi}_4\text{TaO}_8\text{Cl}-\text{F}$ (Fig. S7b) while the thermal decomposition method leads to randomly distributed CoO_x particles with $\text{Bi}_4\text{TaO}_8\text{Cl}-\text{F}$ (Fig. S7c). For discrimination, CoO_x deposited $\text{Bi}_4\text{TaO}_8\text{Cl}-\text{F}$ via the hydrothermal method, photo-deposition method, and thermal decomposition method are labeled as $\text{CoO}_x(\text{H})@\text{Bi}_4\text{TaO}_8\text{Cl}-\text{F}$, $\text{CoO}_x(\text{P})@\text{Bi}_4\text{TaO}_8\text{Cl}-\text{F}$, and $\text{CoO}_x(\text{T})@\text{Bi}_4\text{TaO}_8\text{Cl}-\text{F}$, respectively. For comparison purposes, the content of CoO_x within these samples was kept the same as 2 wt%.

3.4. Photocatalytic performance after cocatalyst deposition

The facet-selective deposition of CoO_x over $\text{Bi}_4\text{TaO}_8\text{Cl}-\text{F}$ by hydrothermal method works quite effectively in improving the photocatalytic activity. Compared with pristine $\text{Bi}_4\text{TaO}_8\text{Cl}-\text{F}$, $\text{CoO}_x(\text{H})@\text{Bi}_4\text{TaO}_8\text{Cl}-\text{F}$ produced almost four-fold O_2 for the 2.5 h reaction time (Fig. 7a), highlighting the pivotal role of CoO_x cocatalyst for water oxidation reactions. However, the efficacy of CoO_x hinges dramatically on the deposition method. CoO_x would have a negligible or deleterious impact on the photocatalytic activity if deposited by photo-deposition or

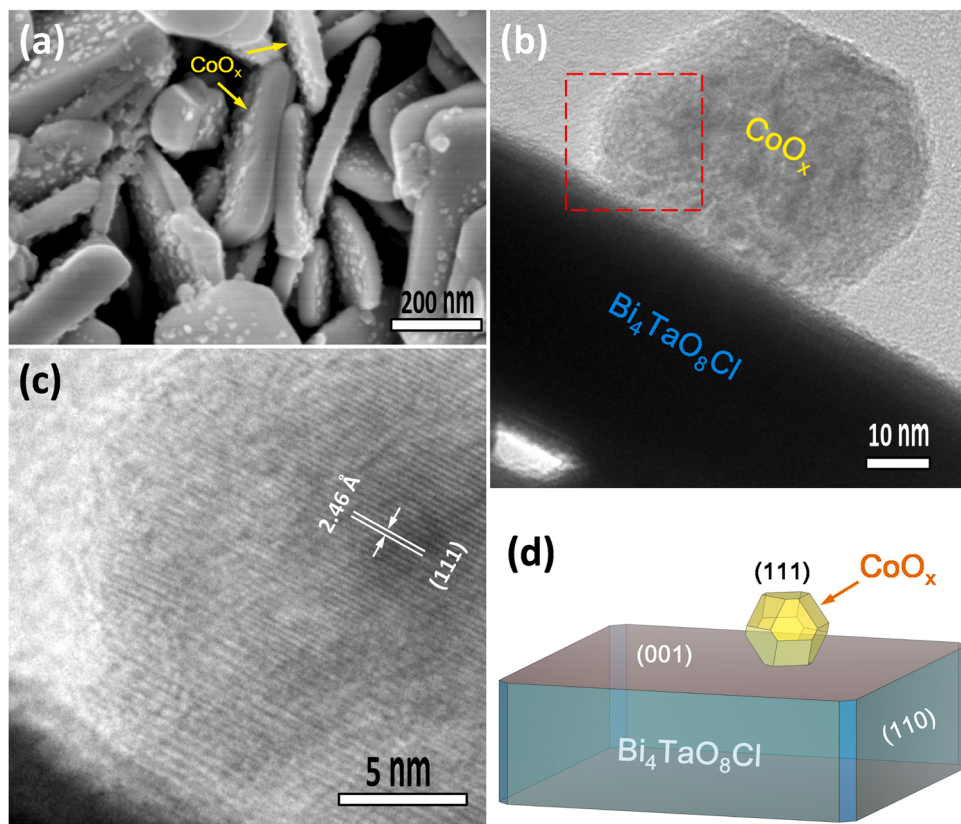


Fig. 6. (a) FE-SEM image of $\text{Bi}_4\text{TaO}_8\text{Cl}$ -F particles deposited with CoO_x by a hydrothermal method, i.e. $\text{CoO}_x(\text{H})@\text{Bi}_4\text{TaO}_8\text{Cl}$ -F. (b) TEM image of $\text{CoO}_x(\text{H})@\text{Bi}_4\text{TaO}_8\text{Cl}$ -F showing attachment between CoO_x and $\text{Bi}_4\text{TaO}_8\text{Cl}$ -F. (c) high-resolution TEM image at the region marked by the red dashed square in (b), lattice fringe marked corresponds to (111) plane of CoO . (d) schematic illustration of contact between $\text{Bi}_4\text{TaO}_8\text{Cl}$ (001) facet and CoO_x (111) facet.

thermal decomposition method (Fig. 7b). Apart from the deposition method, the content of CoO_x is another important parameter to modulate the activity. Optimal content of 2 wt% has been found for CoO_x deposited by the hydrothermal method (Fig. 7c). Under these optimal conditions, the action spectrum for photocatalytic water oxidation has been collected which are illustrated in Fig. 7d. The action spectrum matches well with the UV-vis absorption spectrum of $\text{Bi}_4\text{TaO}_8\text{Cl}$ -F and has an onset around 500 nm, indicating that water oxidation over $\text{CoO}_x(\text{H})@\text{Bi}_4\text{TaO}_8\text{Cl}$ -F is essentially photon-driven and proceeds via bandgap excitations. An apparent quantum efficiency as high as 27% at 420 ± 20 nm has been recorded and stands as the highest value for this kind of photocatalyst reported to date, to the best of our knowledge (Table S3). Nevertheless, photocatalytic overall water splitting have not been achieved in $\text{Bi}_4\text{TaO}_8\text{Cl}$ -F albeit cocatalysts can be facet-selectively deposited. This is probably due to the challenges to modulate both oxidation and reduction reactions simultaneously on $\text{Bi}_4\text{TaO}_8\text{Cl}$ -F given the copious surface states on {110} facets. As water oxidation half-reactions are generally considered as the bottleneck for the overall water splitting reactions, a high activity of water oxidation is therefore extremely useful for the construction of a Z-scheme system. This is exemplified by combining $\text{CoO}_x(\text{H})@\text{Bi}_4\text{TaO}_8\text{Cl}$ -F with $\text{SrTiO}_3\text{:Rh}$, a p-type H_2 -evolution photocatalyst. Mediated by $\text{Fe}^{2+}/\text{Fe}^{3+}$ redox couple, the so-formed the Z-scheme system can split water stably into H_2 and O_2 with correct stoichiometry under both visible light and simulated AM 1.5 illuminations (Fig. 7e and Fig. S8). It is worth noting that $\text{Bi}_4\text{TaO}_8\text{Cl}$ -F now delivers more than a five-fold increment of activity than $\text{Bi}_4\text{TaO}_8\text{Cl}$ -S for Z-scheme overall water splitting, signifying the importance of facet-engineering techniques in opening up the photocatalytic potential of a semiconductor.

3.5. Interplay between cocatalyst and $\text{Bi}_4\text{TaO}_8\text{Cl}$

Considering the distinct microstructures, CoO_x deposited by different methods has been further investigated. Fig. 8a shows the XPS spectra of Bi 4f state for samples prepared by different deposition methods. The Bi 4f state of all samples contains a spin-orbit pair assignable to Bi 4f_{5/2} and Bi 4f_{7/2} states of Bi^{3+} species. The binding energy of these states, however, varies differently among these deposition methods, indicating a variant interplay between CoO_x and $\text{Bi}_4\text{TaO}_8\text{Cl}$ -F. $\text{CoO}_x(\text{H})@\text{Bi}_4\text{TaO}_8\text{Cl}$ -F has its Bi states blue-shifted relative to pristine $\text{Bi}_4\text{TaO}_8\text{Cl}$ -F, suggesting that the $\text{Bi}_4\text{TaO}_8\text{Cl}$ -F substrate is “positively” biased upon hydrothermally depositing CoO_x cocatalyst. This helps to explain its improved photocatalytic activity due to an enlarged depletion layer that promotes photocarrier separation. In contrast, $\text{CoO}_x(\text{P})@\text{Bi}_4\text{TaO}_8\text{Cl}$ -F has its Bi states red-shifted compared to pristine $\text{Bi}_4\text{TaO}_8\text{Cl}$ -F, indicating a “negatively” biased $\text{Bi}_4\text{TaO}_8\text{Cl}$ -F substrate upon photo-depositing CoO_x cocatalyst. This observation is consistent with its poor photocatalytic activity due to a diminished depletion layer that degrades photocarrier separation. As for $\text{CoO}_x(\text{T})@\text{Bi}_4\text{TaO}_8\text{Cl}$ -F, the Bi states have no discernable changes before and after cocatalyst deposition, implying very weak interaction between $\text{Bi}_4\text{TaO}_8\text{Cl}$ -F substrate and CoO_x cocatalyst. This is in good accordance with its microstructures that show random distribution between CoO_x and $\text{Bi}_4\text{TaO}_8\text{Cl}$ -F particles. Similar observations can be seen in the XPS spectra of other constituent elements of $\text{Bi}_4\text{TaO}_8\text{Cl}$ -F (Fig. S9). In addition, electrochemical impedance spectra reveal different interfacial charge transfer resistance associated with the deposition method for CoO_x . The hydrothermal method leads to the smallest interfacial charge transfer resistance while thermal decomposition results in the largest, being consistent with the photocatalytic activity observed and confirming again that the CoO_x deposition method plays a pivotal role here. The

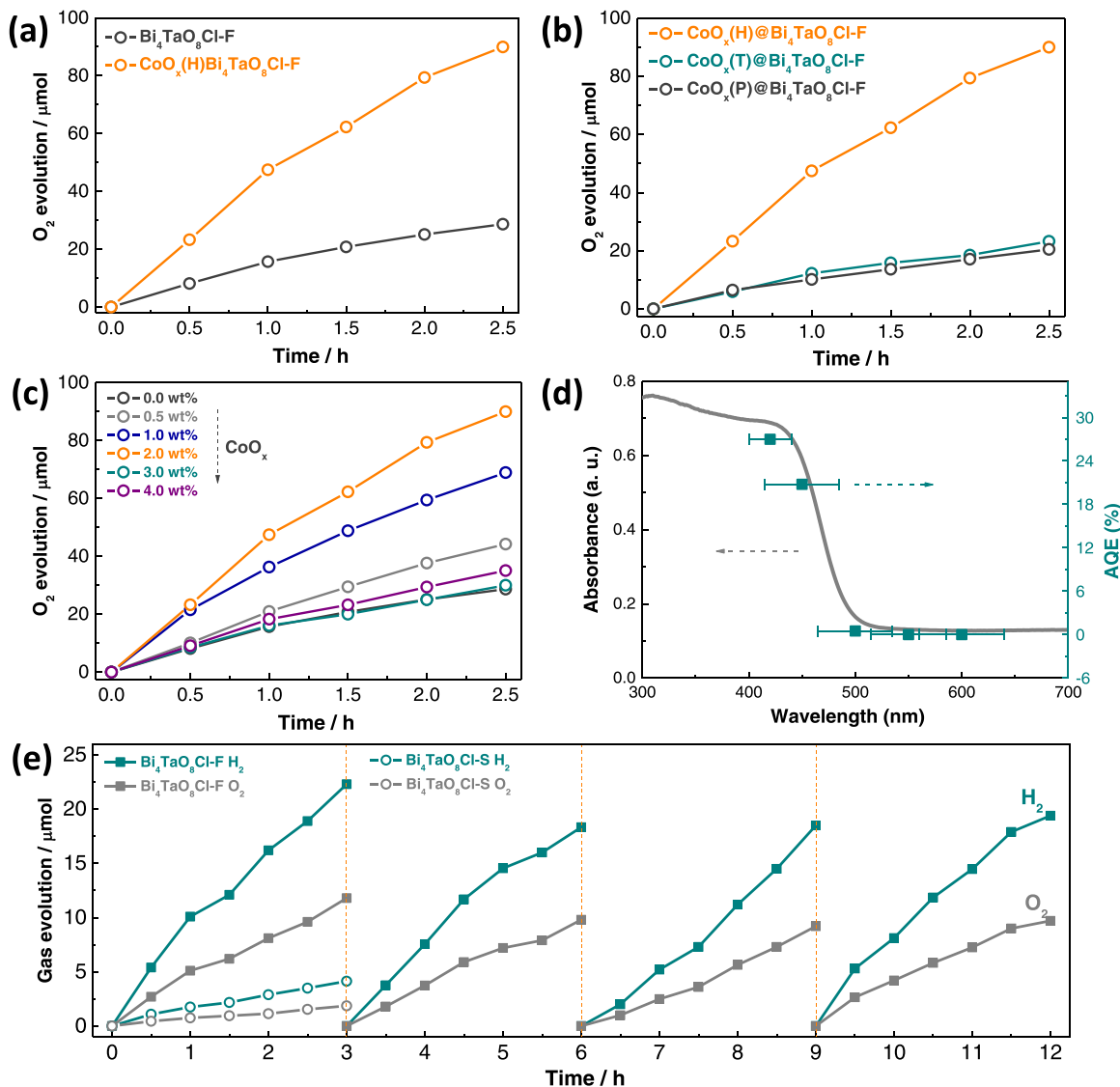


Fig. 7. (a) Photocatalytic O_2 -evolution profile of $\text{Bi}_4\text{TaO}_8\text{Cl-F}$ and $\text{CoO}_x(\text{H})@\text{Bi}_4\text{TaO}_8\text{Cl-F}$. (b) photocatalytic O_2 -evolution profile of $\text{CoO}_x(\text{H})@\text{Bi}_4\text{TaO}_8\text{Cl-F}$, $\text{CoO}_x(\text{T})@\text{Bi}_4\text{TaO}_8\text{Cl-F}$ and $\text{CoO}_x(\text{P})@\text{Bi}_4\text{TaO}_8\text{Cl-F}$. (c) photocatalytic O_2 -evolution profile of $\text{CoO}_x(\text{H})@\text{Bi}_4\text{TaO}_8\text{Cl-F}$ with different CoO_x content. (d) action spectrum of $\text{CoO}_x(\text{H})@\text{Bi}_4\text{TaO}_8\text{Cl-F}$ for photocatalytic O_2 -evolution, UV-vis DRS spectrum was included. (e) Z-scheme overall water splitting under visible light illumination ($\lambda \geq 420 \text{ nm}$) over $\text{CoO}_x(\text{H})@\text{Bi}_4\text{TaO}_8\text{Cl-F}$ (50 mg), $\text{SrTiO}_3:\text{Rh}$ (50 mg) and $\text{Fe}^{2+}/\text{Fe}^{3+}$ redox couple (0.002 M), the system was degassed every 3 h. $\text{Bi}_4\text{TaO}_8\text{Cl-S}$ is also included for comparisons and is tested under identical conditions.

superior photocatalytic performance of $\text{CoO}_x(\text{H})@\text{Bi}_4\text{TaO}_8\text{Cl-F}$ can then be understood by the much-improved charge separation efficiency as well as facile interfacial charge transfer, as has been confirmed by PEC analysis (Fig. 8c and Fig. 8d).

To get a deeper insight as to how photocarriers are dispersed, the photocarriers distribution inside $\text{Bi}_4\text{TaO}_8\text{Cl-F}$ before and after CoO_x deposition has been simulated. Fig. 9 illustrates the electrons and holes concentration over the cross-section of a single $\text{Bi}_4\text{TaO}_8\text{Cl-F}$ plate-like particle under visible light illumination. Thanks to the differences in energy states between $\{001\}$ and $\{110\}$ facets, photocarriers are unevenly dispersed at the cross-section of $\text{Bi}_4\text{TaO}_8\text{Cl-F}$ particle. Electrons clearly have a high concentration at regions close to the $\{110\}$ facet and holes to the $\{001\}$ facet, i.e. the facet-assisted photocarrier separation. However, although photocarriers are well-separated at regions near the surface, they are poorly separated at the center of the particle where holes, in particular, have a high concentration. Only by depositing CoO_x at $\{001\}$ facets can these photocarriers be further separated at both surface and center of $\text{Bi}_4\text{TaO}_8\text{Cl-F}$ particle. Under this circumstance, holes are accumulated at regions deposited with CoO_x cocatalyst where

water oxidation reactions can proceed smoothly. These simulations evidently reveal the crucial roles of crystal facets and facet-selective CoO_x deposition in steering the flow of photocarriers in $\text{Bi}_4\text{TaO}_8\text{Cl-F}$ and well-explains its exceptional photocatalytic performance for water oxidation into O_2 .

4. Conclusions

We have identified a facet-assisted mechanism for photocarrier separation in flux-treated $\text{Bi}_4\text{TaO}_8\text{Cl}$ crystals that exposes mainly $\{001\}$ and $\{110\}$ facets. The distinct atomic arrangements at $\{001\}$ and $\{110\}$ facets result in different energy states that form an internal electric field for the separation of photocarriers to different crystal facets. Thanks to the facet-assisted photocarrier separation, flux-treated $\text{Bi}_4\text{TaO}_8\text{Cl}$ owns a much higher photocatalytic activity than conventionally prepared one for water oxidation reactions. We have further taken advantage of this phenomenon by depositing CoO_x cocatalyst at $\{001\}$ facets to which holes are driven, i.e. facet-selective cocatalyst deposition. This is realized by a hydrothermal method that generates CoO_x nanoparticles

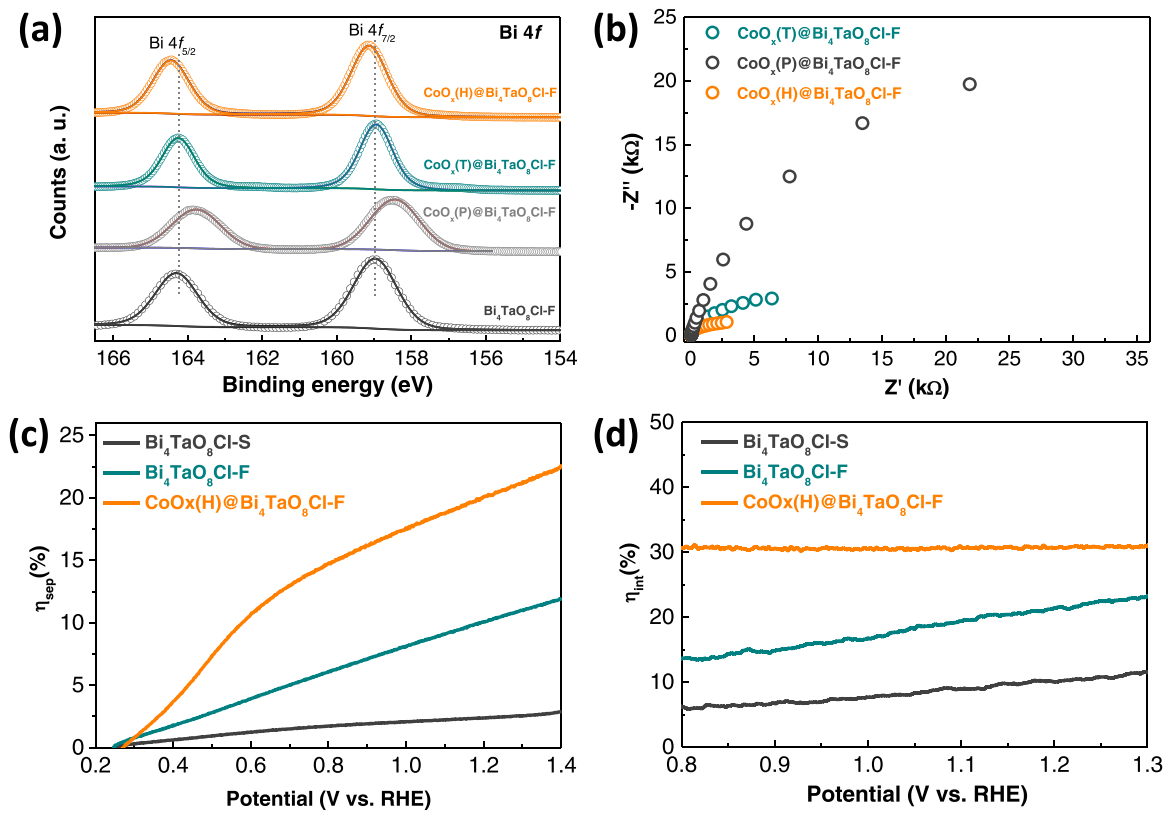


Fig. 8. (a) XPS Bi 4f state of Bi₄TaO₈Cl-F, CoO_x(H)@Bi₄TaO₈Cl-F, CoO_x(T)@Bi₄TaO₈Cl-F and CoO_x(P)@Bi₄TaO₈Cl-F. (b) Nyquist plot of impedance spectra of CoO_x(H)@Bi₄TaO₈Cl-F, CoO_x(T)@Bi₄TaO₈Cl-F and CoO_x(P)@Bi₄TaO₈Cl-F under visible light illumination ($\lambda \geq 420$ nm). (c) charge separation efficiency (η_{sep}) at different potentials of Bi₄TaO₈Cl-S, Bi₄TaO₈Cl-F and CoO_x(H)@Bi₄TaO₈Cl-F. (d) interfacial charge transfer (η_{int}) at different potentials of Bi₄TaO₈Cl-S, Bi₄TaO₈Cl-F and CoO_x(H)@Bi₄TaO₈Cl-F.

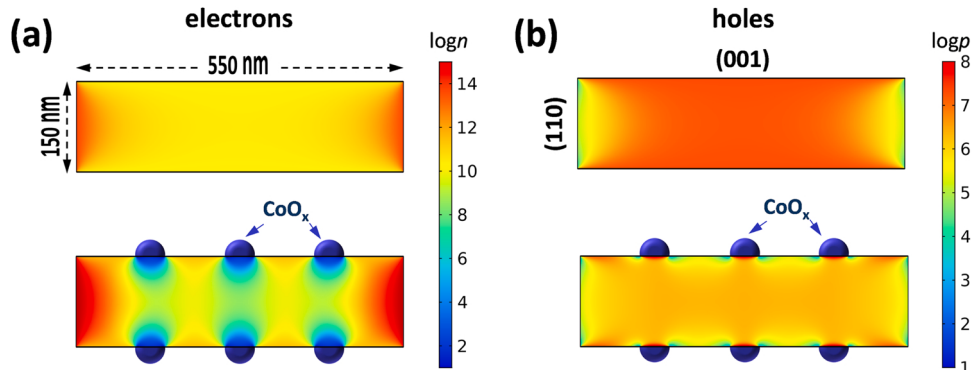


Fig. 9. Photocarrier distribution over the cross-section of Bi₄TaO₈Cl-F plates before and after CoO_x under visible light illumination ($\lambda \geq 420$ nm): (a) electrons. (b) holes.

exclusively and homogeneously at {001} facets of Bi₄TaO₈Cl. Compared with conventional deposition methods, the hydrothermal method enables a strong interplay between cocatalyst and substrate that facilitates the separation, collection, and interfacial transfer of photocarriers. The combination of the two facet-engineering techniques offers collectively control over the flow of photocarriers which cascade continuously from bulk to the surface for water oxidation reactions. Under optimal conditions, the CoO_x deposited Bi₄TaO₈Cl achieves an unprecedentedly high apparent quantum efficiency of 27% at 420 ± 20 nm for water oxidation into O₂. The application of the photocatalyst is also exemplified by constructing a Z-scheme system that enables stable overall water splitting into stoichiometric H₂ and O₂ under visible light illumination. The strategy of facet-selective cocatalyst deposition is very promising to

the improvement of catalytic levels of other photocatalysts as reduction/oxidation reaction sites can be spatially separated.

CRediT authorship contribution statement

Shufang Chang: Investigation, Methodology, and Data curation; **Li Shi:** Formal analysis, Investigation; **Jinxing Yu:** Investigation, Methodology, Data curation; **Ran Wang:** Data curation; **Xiaoxiang Xu:** Funding acquisition, Project administration, Resources, Software, Supervision, Validation, Writing – original draft, Writing – review & editing; **Gang Liu:** Project administration, Resources, Supervision, Validation, Writing – original draft, Writing – review & editing.

Declaration of Competing Interest

The authors declare that they have no known competing financial interests or personal relationships that could have appeared to influence the work reported in this paper.

Data Availability

Data will be made available on request.

Acknowledgements

We thank the National Natural Science Foundation of China (Grant No. 51972233, 52172225, 51825204, 22203046), Science and Technology Commission of Shanghai Municipality (Grant No. 19DZ2271500), Shanghai Sailing Program (Grant No. 22YF1447900) and the Fundamental Research Funds for the Central Universities for funding. Gang Liu thanks the support from the National Key R & D Program of China (No.2021YFA1500800).

Appendix A. Supporting information

Supplementary data associated with this article can be found in the online version at [doi:10.1016/j.apcatb.2023.122541](https://doi.org/10.1016/j.apcatb.2023.122541).

References

- [1] S.S. Chen, T. Takata, K. Domen, Particulate photocatalysts for overall water splitting, *Nat. Rev. Mater.* 2 (2017) 17050, <https://doi.org/10.1021/acsnanolett.8b02209>.
- [2] D.M. Zhao, Y.Q. Wang, C.L. Dong, Y.C. Huang, J. Chen, F. Xue, S.H. Shen, L.J. Guo, Boron-doped nitrogen-deficient carbon nitride-based Z-scheme heterostructures for photocatalytic overall water splitting, *Nat. Energy* 6 (2021) 388–397, <https://doi.org/10.1038/s41560-021-00795-9>.
- [3] Y.Q. Sheng, W.L. Li, L.L. Xu, Y.F. Zhu, High photocatalytic oxygen evolution via strong built-in electric field induced by high crystallinity of perylene imide supramolecule, *Adv. Mater.* 34 (2022), 2102354, <https://doi.org/10.1002/adma.202102354>.
- [4] P. Salcedo-Abraira, A.A. Babaryk, E. Montero-Lanzuela, O.R. Contreras-Almengor, M. Cabrero-Antonino, E.S. Grape, T. Willhammar, S. Navalón, E. Elkaim, H. García, P. Horcajada, A novel porous Ti-Squareate as efficient photocatalyst in the overall water splitting reaction under simulated sunlight irradiation, *Adv. Mater.* 33 (2021) 2106627, <https://doi.org/10.1002/adma.202106627>.
- [5] J. Yang, J.F. Jing, Y.F. Zhu, A. Full-Spectrum Porphyrin-Fullerene, D.-A. Supramolecular Photocatalyst, A full-spectrum porphyrin-fullerene D.-A. supramolecular photocatalyst with giant built-in electric field for efficient hydrogen production, *Adv. Mater.* 33 (2021) 2101026, <https://doi.org/10.1002/adma.202101026>.
- [6] C. Cheng, B.W. He, J.J. Fan, B. Cheng, S.W. Cao, J.G. Yu, An inorganic/organic s-scheme heterojunction H₂-production photocatalyst and its charge transfer mechanism, *Adv. Mater.* 33 (2021) 2100317, <https://doi.org/10.1002/adma.202100317>.
- [7] T. Takata, J.Z. Jiang, Y. Sakata, M. Nakabayashi, N. Shibata, V. Nandal, K. Seki, T. Hisatomi, K. Domen, Photocatalytic water splitting with a quantum efficiency of almost unity, *Nature* 581 (2020) 411–414, <https://doi.org/10.1038/s41586-020-2278-9>.
- [8] H. Kato, K. Asakura, A. Kudo, Highly efficient water splitting into H₂ and O₂ over lanthanum-doped NaTaO₃ photocatalysts with high crystallinity and surface nanostructure, *J. Am. Chem. Soc.* 125 (2003) 3082–3089, <https://doi.org/10.1021/ja027751g>.
- [9] K. Takanabe, Photocatalytic water splitting: quantitative approaches toward photocatalyst by design, *ACS Catal.* 7 (2017) 8006–8022, <https://doi.org/10.1021/acscatal.7b02662>.
- [10] H. Fujito, H. Kunioku, D. Kato, H. Suzuki, M. Higashi, H. Kageyama, R. Abe, Layered perovskite oxychloride Bi₄NbO₈Cl: a stable visible light responsive photocatalyst for water splitting, *J. Am. Chem. Soc.* 138 (2016) 2082–2085, <https://doi.org/10.1021/jacs.5b11191>.
- [11] A.M. Kusainova, W.Z. Zhou, J.T.S. Irvine, P. Lightfoot, Layered intergrowth phases Bi₄MO₈X (X = Cl, M = Ta, and X = Br, M = Ta or Nb): Structural and electrophysical characterization, *J. Solid State Chem.* 166 (2002) 148–157, <https://doi.org/10.1006/jssc.2002.9572>.
- [12] A.M. Kusainova, S.Y. Stefanovich, V.A. Dolgikh, A.V. Mosunov, C.H. Hervoches, P. Lightfoot, Dielectric properties and structure of Bi₄NbO₈Cl and Bi₄TaO₈Cl, *J. Mater. Chem.* 11 (2001) 1141–1145, <https://doi.org/10.1039/b008492l>.
- [13] D. Kato, K. Hongo, R. Maezono, M. Higashi, H. Kunioku, M. Yabuuchi, H. Suzuki, H. Okajima, C.C. Zhong, K. Nakano, R. Abe, H. Kageyama, Valence band engineering of layered bismuth oxyhalides toward stable visible-light water splitting: madelung site potential analysis, *J. Am. Chem. Soc.* 139 (2017) 18725–18731, <https://doi.org/10.1021/jacs.7b11497>.
- [14] H. Kunioku, M. Higashi, O. Tomita, M. Yabuuchi, D. Kato, H. Fujito, H. Kageyama, R. Abe, Strong hybridization between Bi-6s and O-2p orbitals in Sillen-Aurivillius perovskite Bi₄MO₈X (M = Nb, Ta; X = Cl, Br), visible light photocatalysts enabling stable water oxidation, *J. Mater. Chem. A* 6 (2018) 3100–3107, <https://doi.org/10.1039/C7TA08619A>.
- [15] D. Kato, R. Abe, H. Kageyama, Extended layer-by-layer Madelung potential analysis of layered oxyhalide photocatalysts and other layered systems, *J. Mater. Chem. A* 7 (2019) 19846–19851, <https://doi.org/10.1039/C9TA05201A>.
- [16] X.P. Tao, Y.Y. Gao, S.Y. Wang, X.Y. Wang, Y. Liu, Y. Zhao, F.T. Fan, M. Dupuis, R. G. Li, C. Li, Interfacial charge modulation: an efficient strategy for boosting spatial charge separation on semiconductor photocatalysts, *Adv. Energy Mater.* 9 (2019) 1803951, <https://doi.org/10.1002/aenm.201803951>.
- [17] X.P. Tao, Y. Zhao, L.C. Mu, S.Y. Wang, R.G. Li, C. Li, Bismuth tantalum oxyhalogen: a promising candidate photocatalyst for solar water splitting, *Adv. Energy Mater.* 8 (2018) 1701392, <https://doi.org/10.1002/aenm.201701392>.
- [18] Z.D. Wei, J.Y. Liu, W.J. Fang, Z. Qin, Z. Jiang, W.F. Shangguan, A visible-light driven novel layered perovskite oxyhalide Bi₄Mo₈X (M = Nb, Ta; X = Cl, Br) constructed using BiOX (X = Cl, Br) for enhanced photocatalytic hydrogen evolution, *Catal. Sci. Technol.* 8 (2018) 3774–3784, <https://doi.org/10.1039/C8CY00959G>.
- [19] Y. You, S.B. Wang, K. Xiao, T.Y. Ma, Y.H. Zhang, H.W. Huang, Z-Scheme g-C₃N₄/Bi₄NbO₈Cl heterojunction for enhanced photocatalytic hydrogen production, *ACS Sustain. Chem. Eng.* 6 (2018) 16219–16227, <https://doi.org/10.1021/acssuschemeng.8b03075>.
- [20] H. Suzuki, M. Higashi, H. Kunioku, R. Abe, A. Saeki, Photoconductivity-lifetime product correlates well with the photocatalytic activity of oxyhalides Bi₄TaO₈Cl and PbBiO₂Cl: an approach to boost their O₂ evolution rates, *ACS Energy Lett.* 4 (2019) 1572–1578, <https://doi.org/10.1016/j.cattod.2017.04.030>.
- [21] A. Nakada, A. Saeki, M. Higashi, H. Kageyama, R. Abe, Two-step synthesis of Sillen-Aurivillius type oxychlorides to enhance their photocatalytic activity for visible-light-induced water splitting, *J. Mater. Chem. A* 6 (2018) 10909–10917, <https://doi.org/10.1039/C8TA03321H>.
- [22] K. Ogawa, A. Nakada, H. Suzuki, O. Tomita, M. Higashi, A. Saeki, H. Kageyama, R. Abe, Flux synthesis of layered oxyhalide Bi₄NbO₈Cl photocatalyst for efficient Z-scheme water splitting under visible light, *Acs Appl. Mater. Inter* 11 (2019) 5642–5650, <https://doi.org/10.1021/acsmami.8b06411>.
- [23] H. Kunioku, A. Nakada, M. Higashi, O. Tomita, H. Kageyama, R. Abe, Improved water oxidation under visible light on oxyhalide Bi₄MO₈X (M = Nb, Ta; X = Cl, Br) photocatalysts prepared using excess halogen precursors, *Sustain. Energ. Fuels* 2 (2018) 1474–1480, <https://doi.org/10.1039/C8SE00097B>.
- [24] X. Zhang, Z.H. Ai, F.L. Jia, L.Z. Zhang, Generalized one-pot synthesis, characterization, and photocatalytic activity of hierarchical BioX (X = Cl, Br, I) nanoplate microspheres, *J. Phys. Chem. C* 112 (2008) 747–753, <https://doi.org/10.1021/jp077471t>.
- [25] C.W. Dong, S.Y. Lu, S.Y. Yao, R. Ge, Z.D. Wang, Z. Wang, P.F. An, Y. Liu, B. Yang, H. Zhang, Colloidal synthesis of ultrathin monoclinic BiVO₄ nanosheets for Z-scheme overall water splitting under visible light, *Acs Catal.* 8 (2018) 8649–8658, <https://doi.org/10.1021/acscatal.8b01645>.
- [26] S.F. Chang, J.X. Yu, R. Wang, Q.Y. Fu, X.X. Xu, LaTaON₂ mesoporous single crystals for efficient photocatalytic water oxidation and Z-scheme overall water splitting, *ACS Nano* 15 (2021) 18153–18162, <https://doi.org/10.1021/acsnano.1c06871>.
- [27] L. Yang, Q.Y. Fu, L.N. Wang, J.X. Yu, X.X. Xu, Liberating photocarriers in mesoporous single-crystalline SrTaO₂N for efficient solar water splitting, *Appl. Catal. B-Environ.* 304 (2022), 120934, <https://doi.org/10.1016/j.apcatb.2021.120934>.
- [28] Y.W. Wang, S.H. Wei, X.X. Xu, SrTaO₂N-CaTaO₂N solid solutions as efficient visible light active photocatalysts for water oxidation and reduction, *Appl. Catal. B-Environ.* 263 (2020), 118315, <https://doi.org/10.1016/j.apcatb.2019.118315>.
- [29] S.H. Wei, S.F. Chang, F. Yang, Z.P. Fu, G. Liu, X.X. Xu, Stable and efficient solar-driven photoelectrochemical water splitting into H₂ and O₂ based on a BaTaO₂N photoanode decorated with CoO microflowers, *Chem. Commun.* 57 (2021) 4412–4415, <https://doi.org/10.1039/D0CC07778J>.
- [30] Y.J. Zhong, Z.S. Li, X. Zhao, T. Fang, H.T. Huang, Q.F. Qian, X.F. Chang, P. Wang, S.C. Yan, Z.T. Yu, Z.G. Zou, Enhanced water-splitting performance of perovskite SrTaO₂N photoanode film through ameliorating interparticle charge transport, *Adv. Funct. Mater.* 26 (2016) 7156–7163, <https://doi.org/10.1002/adfm.201603021>.
- [31] G. Kresse, J. Furthmüller, Efficient iterative schemes for ab initio total-energy calculations using a plane-wave basis set, *Phys. Rev. B* 54 (1996) 11169–11186, <https://doi.org/10.1103/PhysRevB.54.11169>.
- [32] G. Kresse, D. Joubert, From ultrasoft pseudopotentials to the projector augmented-wave method, *Phys. Rev. B* 59 (1999) 1758–1775, <https://doi.org/10.1103/PhysRevB.59.1758>.
- [33] J.P. Perdew, J.A. Chevary, S.H. Vosko, K.A. Jackson, M.R. Pederson, D.J. Singh, C. Fiolhais, Atoms, molecules, solids, and surfaces - applications of the generalized gradient approximation for exchange and correlation, *Phys. Rev. B* 46 (1992) 6671–6687, <https://doi.org/10.1103/PhysRevB.46.6671>.
- [34] J.P. Perdew, Y. Wang, Accurate and simple analytic representation of the electron-gas correlation-energy, *Phys. Rev. B* 45 (1992) 13244–13249, <https://doi.org/10.1103/PhysRevB.45.13244>.
- [35] P.E. Blochl, Projector augmented-wave method, *Phys. Rev. B* 50 (1994) 17953–17979, <https://doi.org/10.1103/PhysRevB.50.17953>.

- [36] A.T. Garcia-Esparza, K. Takanabe, A simplified theoretical guideline for overall water splitting using photocatalyst particles, *J. Mater. Chem. A* 4 (2016) 2894–2908, <https://doi.org/10.1039/c5ta06983a>.
- [37] L. Huang, X.L. Wang, J.H. Yang, G. Liu, J.F. Han, C. Li, Dual cocatalysts loaded type I CdS/ZnS core/shell nanocrystals as effective and stable photocatalysts, H₂ Evolution, *J. Phys. Chem. C* 117 (2013) 11584–11591, <https://doi.org/10.1021/jp400010z>.
- [38] G.D. Gilliland, Photoluminescence spectroscopy of crystalline semiconductors, *Mat. Sci. Eng. R* 18 (1997) 99–399, [https://doi.org/10.1016/S0927-796X\(97\)80003-4](https://doi.org/10.1016/S0927-796X(97)80003-4).